A RELATIONSHIP BETWEEN TRANSITION REGION BRIGHTENINGS, ABUNDANCES, AND MAGNETIC TOPOLOGY

LYNDSAY FLETCHER[1,*], MARCELO C. LÓPEZ FUENTES[2], CRISTINA H. MANDRINI[2], BRIGITTE SCHMIEDER[3], PASCAL DÉMOULIN[3], HELEN E. MASON[4], PETER R. YOUNG[5] and NARIAKI NITTA[1]

[1]*Lockheed Martin Solar and Astrophysics Lab., Org L9-41, B252, 2351 Hanover Street, Palo Alto CA 94306, U.S.A. (e-mail: fletcher@sag.lmsal.com)*

[2]*Instituto de Astronomía y Física del Espacio, IAFE, CC67, Suc 28, 1428 Buenos Aires, Argentina*

[3]*Observatoire de Paris, 92195 Meudon, Cedex Principal, France*

[4]*Department of Applied Mathematics and Theoretical Physics, Cambridge University, Silver Street, Cambridge CA, UK*

[5]*Harvard Smithsonian Center for Astrophysics, 60 Garden St., Cambridge, MA 02138, U.S.A.*

(Received 18 November 2000; accepted 14 March 2001)

Abstract. We present multi-instrument observations of active region (AR) 8048, made between 3 June and 5 June 1997, as part of the SOHO Joint Observing Program 33. This AR has a sigmoid-like global shape and undergoes transient brightenings in both soft X-rays and transition region (TR) lines. We compute a magneto-hydrostatic model of the AR magnetic field, using as boundary condition the photospheric observations of SOHO/MDI. The computed large-scale magnetic field lines show that the large-scale sigmoid is formed by two sets of coronal loops. Shorter loops, associated with the core of the SXT emission, coincide with the loops observed in the hotter CDS lines. These loops reveal a gradient of temperature, from 2 MK at the top to 1 MK at the ends. The field lines most closely matching these hot loops extend along the quasi-separatrix layers (QSLs) of the computed coronal field. The TR brightenings observed with SOHO/CDS can also be associated with the magnetic field topology, both QSL intersections with the photosphere, and places where separatrices issuing from bald patches (sites where field lines coming from the corona are tangent to the photosphere) intersect the photosphere. There are, furthermore, suggestions that the element abundances measured in the TR may depend on the type of topological structure present. Typically, the TR brightenings associated with QSLs have coronal abundances, while those associated with BP separatrices have abundances closer to photospheric values. We suggest that this difference is due to the location and manner in which magnetic reconnection occurs in two different topological structures.

1. Introduction

Even simple solar active regions pose many questions, regarding their formation, structure and evolution. In this work, we present observations made during a three-day study of AR 8048, using space- and ground-based instrumentation. The analysis of the coronal and transition region (TR) manifestations of this AR, coupled

*Now at Department of Astronomy and Astrophysics, University of Glasgow, Glasgow G12 8QQ, UK (e-mail: lyndsay@astro.gla.ac.uk).

Solar Physics **203:** 255–287, 2001.

with the modeling of the magnetic field illuminates many aspects of the evolution of the AR, both on the scale of the large loops and small scale brightenings.

The Joint Observing Program 33 (JOP 33) was an observing campaign of the Solar and Heliospheric Observatory (SOHO) that ran between 3 June and 5 June 1997. It involved the Coronal Diagnostic Spectrometer (CDS) (Harrison *et al.*, 1991), the Extreme Ultraviolet Imaging Telescope (EIT) (Delaboudinière *et al.*, 1995) and the Michelson Doppler Interferometer (MDI) (Scherrer *et al.*, 1995). Also participating in this campaign were the Soft X-ray Telescope (SXT) on board *Yohkoh* (Tsuneta *et al.*, 1991; Ogawara *et al.*, 1991) and the Bialków Hα telescope in Poland. This group of instruments provided us with plasma diagnostics, magnetic field measurements, and high and low temperature images of AR 8048.

AR 8048 was a well-isolated region with a sigmoidal appearance, i.e., on the large scale its loops had a sinuous form. Such sigmoidal features were identified by Nakagawa (1971), as being loops with a high twist or helicity. Rust and Kumar (1996) and Hudson *et al.* (1998) found that, in many cases, the ejection of coronal material (as observed by *Yohkoh*/SXT) is associated with bright sigmoids, which evolve into arcades of bright loops and which may undergo several eruptions, indicating the release of stored magnetic energy. In fact, repeated eruptions were observed in AR 8048. However, as is described in Section 4.2, the sigmoidal shape of the large-scale loops in our AR can be matched well by a nearly potential model. This suggests that the large-scale sigmoidicity of this AR may not be a sign of helicity, but of complexity of the magnetic configuration.

The CDS spectroheliograms reveal a characteristically dynamic TR, with sources varying on the most rapid time scales studied (10–20 min). Some of these sources can be readily associated with hotter coronal structures, for example mapping the ends of core SXT loops (as in the case of Mg IX 368.1 Å at 1 MK). However, in lines formed in the temperature range 0.4 MK to 0.8 MK the emission often occurs in locations having no clear coronal counterpart. This emission is sometimes in the form of compact sources, only 6–9 arc sec across; sometimes in long, narrow emission patterns. This looks quite unlike what is seen at higher temperatures (see, for example, Figure 1).

Our CDS data include a number of lines from ions of Mg and Ne, providing the opportunity to investigate the Mg/Ne abundance ratio. Mg and Ne are examples of low and high first ionization potential ions (FIPs of 7.6 and 21.6 eV, respectively). It has been known for some time that the abundances of low FIP relative to high FIP ions is higher in the corona than in the photosphere (Meyer, 1985a, b). Spatially resolved spectral observations show that coronal values of the ratio are found in spiky structures extending outwards from the strong magnetic fields of ARs – possibly the base of coronal loops – while photospheric values are found in (morphologically different) strong isolated TR brightenings (Young and Mason, 1997; Sheeley, 1996).

The brightness distribution at various temperatures, and possibly also the element abundances, are likely to be linked to the magnetic configuration, since the

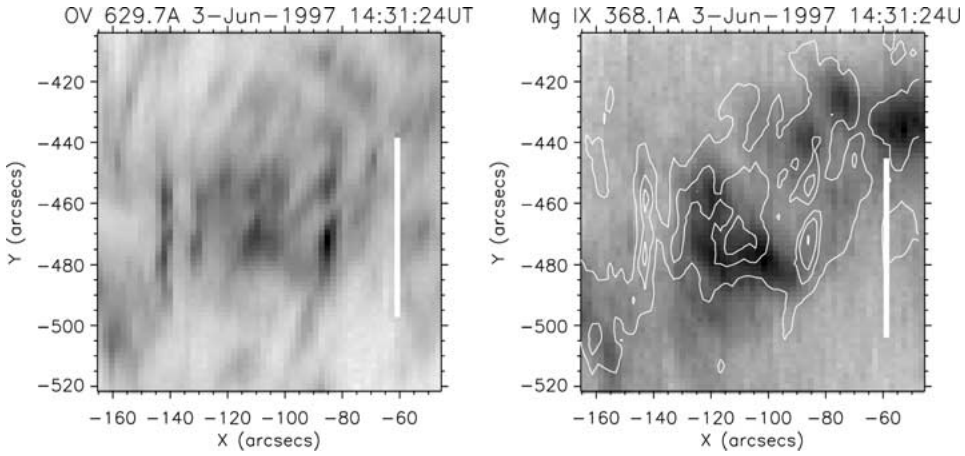

Figure 1. AR 8048 viewed in O V 629.7 Å, a transition region line formed at 0.25 MK, and Mg IX at 368.1 Å, a transition region/coronal line formed at 1 MK. Overlaying the O V contours on Mg IX illustrates the difference in the type of structure observed. At 0.25 MK, emission is concentrated into small bright blobs and elongated structures, while at 1 MK, emission is far more widespread and diffuse.

magnetic field determines the channels for plasma and energy transport. Motivated by this, we compute the coronal magnetic field from MDI magnetograms and study the magnetic topology, both loop shapes and the locations of critical structures in the field such as 'bald patches' and 'quasi-separatrix layers', which are important for understanding magnetic reconnection.

The conventional view of magnetic reconnection is mainly based on the 2-D picture of an X-type neutral point, or its extension to 3-D. It is thought to be accompanied by flux transport across separatrices, where the field-line mapping is discontinuous. But magnetic reconnection can also occur in two other topologies, as described below.

In the first configuration, field lines coming from the corona, touch tangentially the photospheric inversion line and then go back into the corona. Due to the characteristic concave pattern of these lines, Titov, Priest, and Démoulin (1993) called these photospheric segments 'bald patches' (BPs). Early examples of BPs were given by Seehafer (1986). Secondly, since many magnetic configurations give rise to flares without showing clear evidence for separatrices, the concept of separatrices has been generalized to 'quasi-separatrix layers' (QSLs), defined as regions where the magnetic field-line linkage changes drastically (Démoulin *et al.*, 1997).

In recent years, the relationship between magnetic separatrices and solar emission has been usefully explored in various wavelength regimes. In non-flaring regions, Sakurai and Wang (1999) and Wang, Wang, and Qiu (1999) found that SXT loops and Hα plage emission are closely associated with the locations of magnetic separatrices, which are likely to be the site of current heating (as, for example, in the minimum current corona model of Longcope, 1996). Not surpris-

ingly, separatrix structures are also important in understanding active phenomena, on all scales. On the very smallest scales, van Ballegooijen *et al.* (1998) found a relationship between the predicted locations of separatrices between photospheric flux elements and G-band bright points, while Mandrini *et al.* (1999a,b) related (in particular) BP separatrices to the evolution of Hα fibrils and surges. Aulanier *et al.* (1998b) found a close correspondence between BP separatrices and Hα and soft X-ray emissions in a small flare. Magnetic reconnection at QSLs has been shown to be at the origin of the energy release in a large variety of events ranging from X flares (e.g., Gaizauskas *et al.*, 1998), to small X-ray bright points (Mandrini *et al.*, 1996) and even to very low energy events associated with radio noise storms and faint brightenings observed by TRACE (Bentley *et al.*, 2000).

Emission in the UV and EUV part of the spectrum has, to our knowledge, been little explored in this respect, but has been shown by the spectroheliographic measurements of SOHO/CDS to be a highly structured and dynamic region. In the UV part of the spectrum, Aulanier *et al.* (1999) studied a filament with SOHO/SUMER, and found Si IV brightenings, indicating energy release at the locations of computed BP separatrices.

In this paper we will continue in the vein of studying the association of solar emission and magnetic structures, emphasizing the relationship of TR brightenings and magnetic topology. By reconstructing the magnetic environment of the AR, we have been able to find a relationship between the high temperature coronal emission in the core of the active region and QSLs, and between TR brightenings and the intersection of QSLs or BP separatrices with the photosphere. We further find that the type of magnetic structure (i.e., a QSL or BP separatrix structure) may affect the local element abundances.

The paper is structured in the following way. In Section 2 we describe the AR and its evolution, in Section 3 we present the small-scale behavior of AR 8048 observed by CDS and the results of the CDS plasma diagnostics, focusing our discussion on the abundance computations. In Section 4 we compute the coronal magnetic field and its topology, based on MDI magnetograms on each of the three days of observation. We relate the CDS observations to the magnetic topology of the AR. The most probable physical origin of the observed brightenings is also discussed in Section 5. The final section presents our conclusions.

2. The Structure and Evolution of AR 8048

2.1. GENERALITIES

AR 8048 appeared at the east limb on 30 May 1997, presumably having emerged some time during the preceding half-rotation. The remnant of this AR, considerably decayed, (in particular, without sunspots) is present in the next solar rotation. Several 'eruptive' events, occurring as sudden brightness enhancements, and distortion

of the loops or appearance of a 'cusp' structure, were observed in SXT data (see 'movie.mpg' on the CD ROM). On 1 June, two optical sub-flares were seen in Hα, while on 2, 3, and 5 June filament disappearance events took place. However, there was no significant GOES activity (class B flares or higher) attributed to this AR.

2.2. THE CORONAL SIGMOID APPEARANCE

At the time of its appearance, AR 8048 consisted of a main and a small trailing bipole (see Figure 2). The SXT loop system appears sigmoidal, with loops joining the two polarities of the leading bipole forming the top part of the 'S', and larger, fainter loops, joining the negative polarity of the leading bipole with the positive polarity of the smaller bipole, forming the bottom part of the 'S'. This is in agreement with the independent study of Glover *et al.* (2000) who classified the AR as 'projected-sigmoidal', meaning that the AR comprises many loops, the projection of which onto the disk causes them to appear sigmoidal. However, at various times the core SXT loops, lying between the polarities of the main bipole, also have a slight 'S' shape, apparently without being composed of different systems of loops (Figure 4). This could be indicative of twist, though of a very low value as shown by the magnetic field model in Section 4.2.

Individual loops or groups of loops brighten and dim on time scales of tens of minutes. It seems plausible that this happens as the magnetic elements in which they are rooted merge, reconnect and split as they are buffeted by convective cells. According to our results in Section 4.3, this reconnection process may occur at QSLs.

2.3. THE PHOTOSPHERIC AND CHROMOSPHERIC DESCRIPTION

During the three days of CDS observations, the magnetic flux stayed constant while the area increased, which is a sign that the AR is in its decay phase (van Driel-Gesztelyi, 1998). The leading spot is surrounded by a moat region, which consists of bipolar elements moving radially away from the main field (moving magnetic features) with the outer edge having the same polarity as the sunspot (Figure 3, right-hand panels). The trailing spot does not exhibit this behavior, though both positive and negative flux concentrations undergo several changes near the southern edge of the spot, e.g., the positive flux breaking off from the trailing spot is advected clockwise and southwards around this spot. A movie of the region made from MDI hourly magnetograms reveals a great deal of splitting and merging activity in this small-scale field, with typical magnetic elements (on a scale of ~ 20 arc sec) retaining their identities for a time scale of a few hours before the next merging, splitting or disappearance. Some of these changes are reflected in small-scale intensity variations observed by CDS in low temperature lines.

Bialków Hα telescope provided filtergrams with 0.5 Å bandpass for the 3 days (Figure 3). The fibrils around the trailing spot present a marked clockwise direction, which is indicative of the sign of the twist in the loops (see Section 4.2). On 5 June,

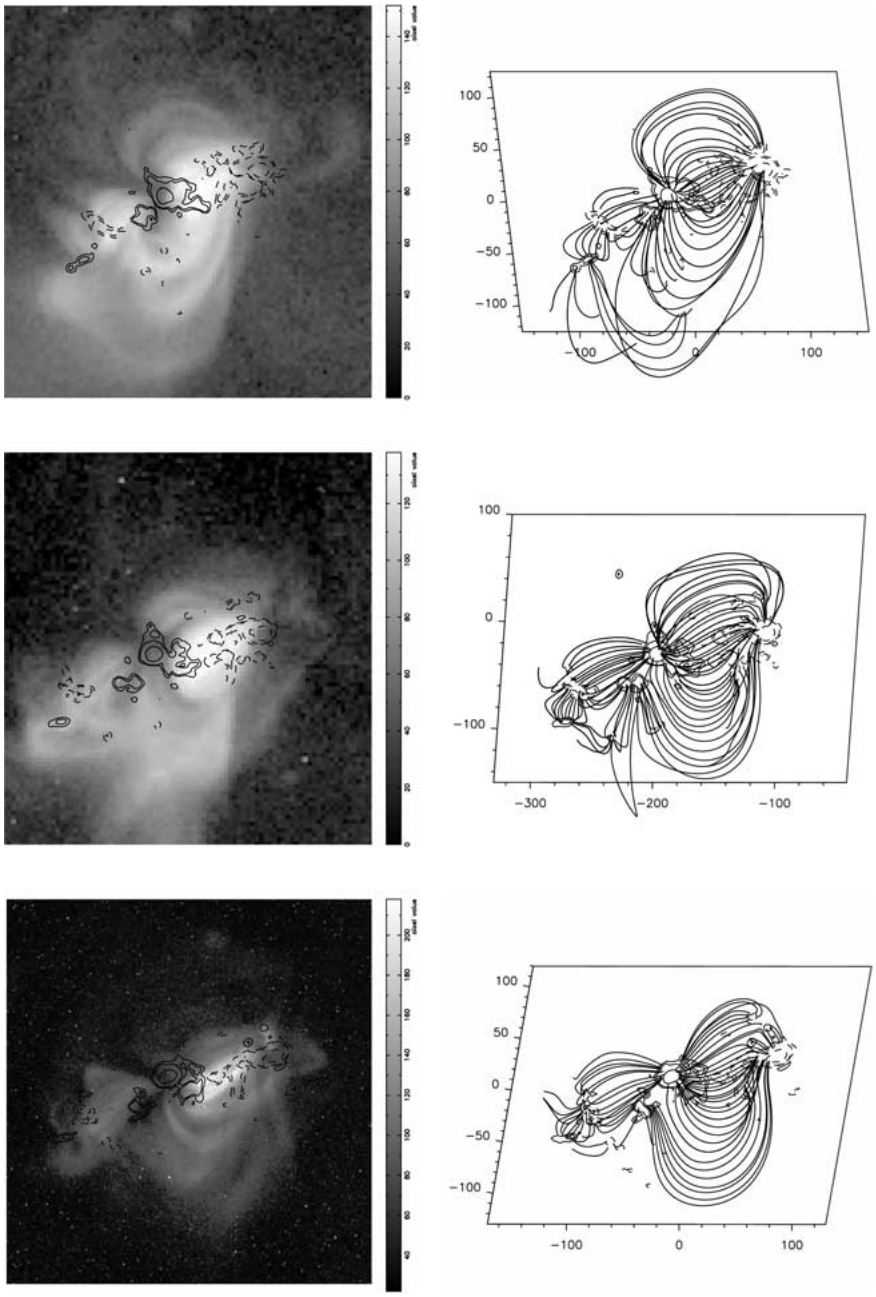

Figure 2. SXT images in Al12 filter (*left column*). The *top row* corresponds to 3 June at 14:08 UT, the *central row* to 4 June at 14:25 UT and the *bottom row* to 5 June at 14:08 UT. The images have been overlaid with MDI magnetograms for comparison with the magnetic model (*right panels*). The MDI magnetograms used correspond to 3 June, 14:28 UT (*top row*), 4 June, 12:52 UT (*central row*) and 5 June, 11:16 UT (*bottom row*). The iso-contours of B_l are $\pm$ 50, 100, and 500 G, positive (negative) values are drawn in *continuous* (*dashed*) line. A set of field lines has been added in every map to be compared with the SXT data. The sizes of the frames are expressed in Mm and the trapezoidal shape is due to the effect of projection.

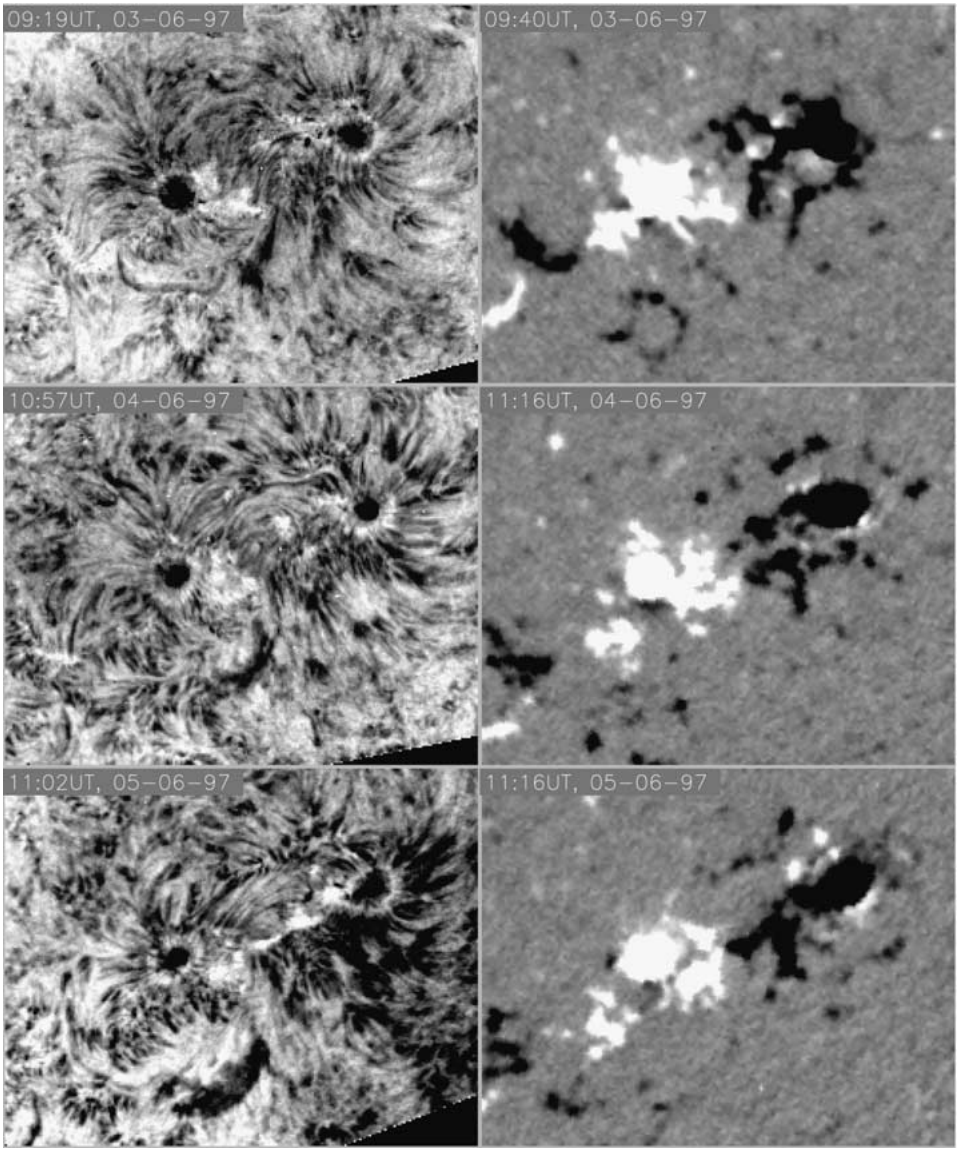

Figure 3. Hα images of Bialków (*left panels*) and MDI magnetograms (*right panels*) for 3, 4, 5 June 1997. The size of the image is $\approx$ 282" in x and 225" in y. *Black* (*white*) represent negative (positive) polarities of the longitudinal field, respectively.

we observed the formation of a filament between the main bipole and the trailing bipolar field.

3. CDS Observations

3.1. CORONAL BRIGHTENINGS

In this section we study the physical properties of AR 8048 on a small scale, using SOHO/CDS data. Spectroheliograms of the AR in a number of lines formed at different temperatures are used to derive abundances and densities, and form a picture of the system at different temperatures.

The CDS field of view covers most of the central portion of AR 8048 on 3 and 4 June, and about half of it on 5 June (Figure 4). We ran two programs - TRANREG and TREG22. TRANREG consists of 5 or 6 rasters, each lasting 10 min, and using a pixel size of 2.0 arc sec $\times$ 1.7 arc sec, in a few strong, well-isolated lines with formation temperatures spanning the range 20 000 K to 2 MK. The TREG22 rasters take approximately 45 min, with a pixel size of 4.0 arc sec $\times$ 1.7 arc sec, in a range of lines spanning TR and low coronal temperatures. In particular, a series of lines from different ionization stages of Mg and Ne are present. The highest temperature line in this raster is the line of Si XII at 520.6 Å with a temperature of maximum ionization fraction of 2 MK. Emission in this ion tends to occur at the same location as the SXT emission in the core of the AR (Figure 4). Emission from locations corresponding to the ends of the hot core loops is present in lines of around one million degrees, e.g., Mg IX. This Mg IX emission is probably the hot upper TR of these overlying high temperature SXT loops – or 'moss', as observed at high resolution by TRACE (e.g., Berger *et al.*, 1999; Fletcher and De Pontieu, 1999). Elongated Mg IX structures are also present, at a low intensity, suggesting the presence of longer loops with a temperature around 1 000 000 deg.

3.2. TRANSITION REGION BRIGHTENINGS AND THEIR EVOLUTION

The distribution of emission in lines of a few hundred thousand K is typically very different from that of lines of 1 MK and above. As an example, a comparison between simultaneous rasters in the strong lines of O V 629.7 Å at 0.25 MK and Mg IX 368.1 Å at 1 MK (Figure 1) shows how, although some of the emission in the lower temperature lines occurs at the same locations as the million degree emission, much of the TR structure has no coronal counterpart. Further, there is no clear association on this scale between the TR line emission and the photospheric field in the region. Rather than thinking in terms of continuous magnetic loops from photosphere to corona, the key to understanding the bright TR emission may in fact lie in the discontinuities – the separatrix structures in the AR magnetic field.

Because of our interest in abundances, we have focused this study on lines of Mg (low FIP) and Ne (high FIP) elements. In TR lines of these elements (e.g., Ne IV, V, VI; Mg V, VI), the emission is concentrated into a small number of intense brightenings.

We identify in the first instance 5 strong Ne VI (562.8 Å) TR brightenings in the TREG22 raster run at 14:09:19 UT on 3 June. These include all pixels around the

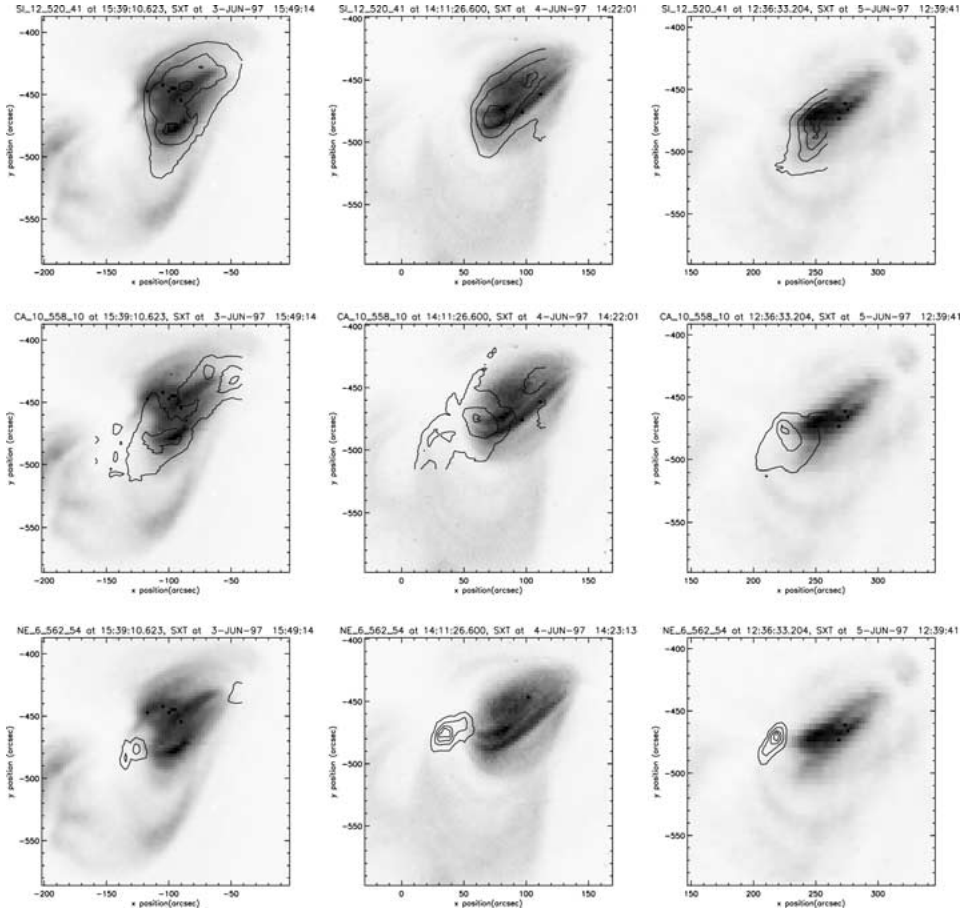

Figure 4. Overlays of SXT AlMg filter image with CDS rasters: Si XII emission ($T = 2 \times 10^6$ K, *first row*), Ca X 557.8 Å emission ($T = 10^6$ K, *middle row*) and Ne VI 562.8 Å emission ($T = 400\,000$ K, *low row*). The Si XII emission follows the bright core of the SXT emission. Ca X emission maps part of the core loops and footpoints, and Ne VI emission is concentrated at the footpoints of the large, diffuse SXT loops. Note that in the observations of 4 and 5 June the CDS raster does not extend to the north end of the SXT loop system.

brightest pixel, more than half of which lie inside the contour corresponding to an intensity in the Ne VI (562.8 Å) line greater than 30 ergs cm^{-2} s^{-1}sterad^{-1}. These are labeled A–E in Figures 9(a) and 12 . These regions were visible in Ne lines from IV to VI. In Mg V, Features A and C were visible; while Features A, C and E were visible in Mg VI. Line intensities in these TR brightenings vary rapidly. Starting at 15:39:10 UT, raster TREG22 is re-run and considerable changes have taken place. In Table I we present the mean intensity, averaged over a number of pixels, from each of the bright features for both runs of the raster on 3 June, obtained by fitting Gaussians plus a constant background to the line profiles averaged over pixels, using χ^2 minimization software written for the purpose by S. V. Haugan.

TABLE I

Intensities in erg $cm^{-2}s^{-1}sterad^{-1}$, averaged over a number of pixels in the low-temperature lines of Ne and Mg on 3 June. For a given feature, the first line is at 14:09:19 UT and the second line at 15:39:10 UT. Note, these intensities are calculated using the CDS NIS calibrations of 23 December 1998.

Feature	Ne IV (543.9 Å)	Ne V (572.3 Å)	Ne VI (562.8 Å)	Mg V (353.2 Å)	Mg VI (349.2 Å)
A	7.6 ± 0.7	15.8 ± 0.5	26.3 ± 0.3	21.8 ± 2.8	37.5 ± 5.2
	2.3 ± 0.2	6.0 ± 0.2	10.8 ± 0.1	7.3 ± 0.9	10.5 ± 1.5
B	6.0 ± 0.6	16.2 ± 0.5	37.9 ± 0.4	12.7 ± 1.6	28.9 ± 4.0
	7.3 ± 0.7	22.0 ± 0.7	45.8 ± 0.5	18.1 ± 2.4	36.5 ± 5.1
C	4.6 ± 0.5	10.9 ± 0.3	26.8 ± 0.3	17.1 ± 0.6	30.6 ± 4.3
	6.0 ± 0.6	18.7 ± 0.6	51.3 ± 0.5	33.5 ± 4.4	78.2 ± 11.0
D	16.6 ± 1.6	21.2 ± 0.6	32.8 ± 0.3	<4.3	17.1 ± 2.4
	9.6 ± 1.0	12.1 ± 0.4	20.5 ± 0.5	109.9 ± 14.2	12.2 ± 1.7
E	5.0 ± 0.5	9.5 ± 0.3	30.2 ± 0.3	12.5 ± 1.6	31.2 ± 4.4
	11 ± 1.1	12.8 ± 0.4	40.9 ± 0.4	65.4 ± 8.5	51.8 ± 7.3

The counts for each of the features at 15:39:19 UT have been averaged over the rotated pixel locations from the 14:09:19 UT observations, regardless of whether these locations are bright in the 15:39:19 UT raster.

The picture is a dynamic one. In the 90-min intervening between the start of each raster, features A and D dim considerably. The intensity of Feature C increases in all of the observed low-temperature lines of Ne and Mg, the increase being higher in the higher-temperature lines. There is also a slight increase in Feature E.

On 4 and 5 June, Features A, C and D are no longer present; while E is no longer in the FOV of CDS (see Figures 9(a), 10(a)). The single Mg/Ne feature appearing on 4 June and 5 June is the same as Feature B on 3 June, this is further borne out by examining the position of the features relative to the MDI magnetic field on subsequent days. This feature first decreases in intensity on 4 June then increases on 5 June (Table II).

Consider the average intensities in Feature C on 3 June (Table I). At 14:09:19 UT they are in the ratio $I_{Ne\,iv} : I_{Ne\,v} : I_{Ne\,vi} = 1 : 3.0 \pm 0.3 : 5.8 \pm 0.6$. At 15:39:10 UT the ratio is $1 : 3.1 \pm 0.3 : 8.6 \pm 0.9$. Emission from high temperature ions has increased relative to that from low temperature ions. This is also seen in the Mg lines. A similar increase in the ratio of intensities is also seen in the single feature (at the location corresponding to B), between the two rasters on 5 June (Table II). By contrast, on 3 June the intensity ratios in Feature B are $1 : 2.7 \pm 0.3 : 6.3 \pm 0.7$ and $1 : 3.0 \pm 0.3 : 6.3 \pm 0.7$ at the two rasters, showing no variation within the errors. How should we interpret these variations?

TABLE II

Intensities in ergs $cm^{-2}s^{-1}$ $sterad^{-1}$, averaged over a number of pixels in the low-temperature lines of Ne and Mg on 4 and 5 June for the only feature present (B).

Date	Ne IV	Ne V	Ne VI	Mg VI	Mg VI
4, 12:16:58	21 ± 1	67 ± 2	163 ± 3	73 ± 2	153 ± 2
4, 14:11:26	14 ± 1	43 ± 1	111 ± 2	42 ± 1	66 ± 2
5, 12:36:33	12 ± 1	43 ± 1	102 ± 2	35 ± 1	68 ± 8
5, 15:02:13	15 ± 1	63 ± 2	180 ± 4	91 ± 3	199 ± 4

The intensity, $I(\lambda_{ji})$ in ergs cm^{-2} s^{-1}, integrated along a given line of sight in a solar plasma is given by

$$4\pi I(\lambda_{ji}) = 0.83 \int_L Ab\, \epsilon_{ij}\, n_e(T_e)\, F(T_e)\, ds, \tag{1}$$

where s is the line-of-sight column depth (the distance L being determined by the range of temperatures, and hence positions in the atmosphere, over which the line is generated), Ab is the abundance of the element relative to hydrogen, $n_e(T_e)$ the electron number density, a function of T_e, the temperature of the local electron distribution (assuming Maxwellians), $F(T_e)$ the ionization fraction for the ion under consideration and 0.83 is the ratio of protons to free electrons. We have defined an ion emissivity, ϵ_{ij} as

$$\epsilon_{ij} = \Delta E\, N_j\, A_{ji}, \tag{2}$$

where ΔE is the photon energy, N_j is the fraction of ions in the upper state j and A_{ji} the Einstein coefficient for the transition. For a collisionally excited line (as is normally assumed to be the case in the optically-thin corona) N_j depends on atomic processes which are a function of the plasma temperature and n_e. So the observed variations in intensity may be due to changes in density, or temperature, or in the abundance of the emitting plasma volume element.

For the case of an isothermal plasma there is of course no variation of n_e with T_e, and if we first consider the ratios of lines from different ionization stages of the same element (e.g., Ne IV, V, VI) then the abundance factors also drop out. So for these lines emitted by an isothermal plasma, the main density dependence of the intensity ratios comes via the ratios of the ϵ_{ij}. For the sequences of magnesium and neon ions considered here, we have used the CHIANTI (v2.0) database (Dere *et al.*, 1997; Landi *et al.*, 1999) to calculate ϵ_{ij} as a function of n_e for the lines that we use, and find the ratios from the different ionization stages vary only by a few percent over the density range $10^9 - 10^{11}$ cm^{-3}. Under the isothermal assumption,

we thus attribute the observed intensity variations within ions of a single element as primarily due to temperature changes, with an increase in emission from a higher ionization stage meaning an increase in the plasma temperature.

We may in fact be dealing with a multi-thermal plasma, with a non-uniform density structure; plane-parallel or otherwise. Attempts have been made to account for the expected variations of temperature and density on line intensities, e.g., within an equilibrium plane parallel atmosphere (e.g., Jordan, 1996), but a more general description for an unspecified density–temperature dependence involves a differential emission measure analysis, which is not performed here.

However, even without making the isothermal assumption, we can learn more about the plasma properties if we consider ratios of lines emitted by ions with the same formation temperature. We can then be fairly certain we are looking at the same emission volumes, even if they are distributed in space throughout the observation pixel(s) and have varying densities. In this case, in a ratio of two line intensities each given by expression (1), where the $F(T_e)$ functions have the same form, the $n_e(T_e)$ dependency will disappear. The principle density dependence of the line ratio then enters via the ratio of the ϵ_{ij}. Further, if one compares lines emitted by different ions with the same formation temperature, and therefore most likely emitted by the same volume of plasma, a primary source of variation in the line emission ratio is abundance variations, as we describe in the following section.

3.3. Determination of Mg/Ne abundance ratios using line ratios

We carry out abundance determinations in each of the bright Ne/Mg features, using two different methods. The first is the line ratio method presented in Young and Mason (1997). Examples of the spectra used for this work are shown in Figure 5.

Writing

$$G(T) = \frac{0.83 N_j \; A_{ji} F(T_e)}{n_e}, \tag{3}$$

Equation (1) becomes

$$4\pi I(\lambda_{ji}) = Ab\Delta E \int_L G(T_e) n_{\mathrm{e}}^2 \, \mathrm{d}s, \tag{4}$$

where $G(T_e)$ is called the contribution function. The line intensity method relies on the fact that the temperature dependence of the $G(T_e)$ functions for the Mg VI 349.2 Å and Ne VI 562.8 Å lines is very similar. In particular, the excitation peak occurs at the same temperature of $\log_{10}(T_e) = 5.62$. If it can be assumed that the emission is occurring in locations where the plasma is at, or very near this peak temperature, and that both lines are emitted by the same volume of plasma, then we can remove the temperature dependence. The ratio of the measured intensities is then directly proportional to the ratio of the elemental abundances.

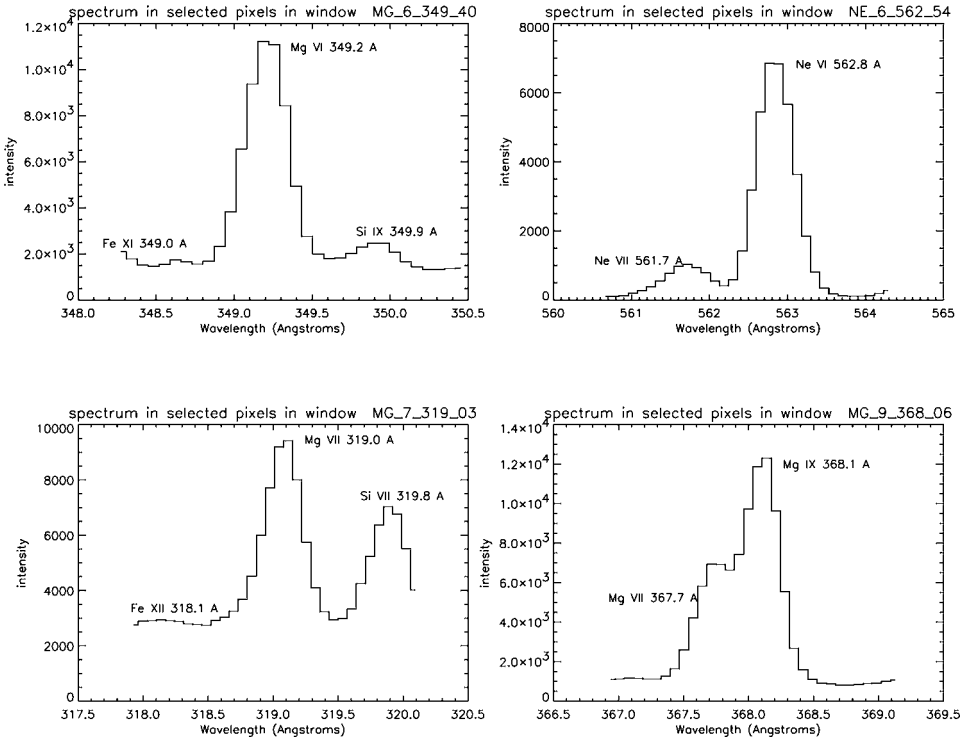

Figure 5. Spectra (counts per second) in the summed pixels in the bright Ne/Mg feature at (35, −475) on 4 June 1997, 12:16:58 UT (see Figure 4) with line identifications. Shown are the Mg VI and Ne VI windows from which the intensity ratio is measured, and the Mg VII and Mg IX windows containing the Mg VII density diagnostic pair.

Under this approximation, the intensity ratio depends on the line emissivities $\epsilon_{349.2}$, $\epsilon_{562.8}$, the ratio Q of the ionization fractions of each ion (calculated at temperature of maximum ionization fraction), and the abundance ratio $R_{\mathrm{Mg/Ne}}$:

$$\frac{I_{349.2}}{I_{562.8}} = \frac{\epsilon_{349.2}}{\epsilon_{562.8}}\, Q\, R_{\mathrm{Mg/Ne}}. \tag{5}$$

Q was estimated by Young and Mason (1997) to have the value 1.22 (on the basis of the Arnaud and Rothenflug (1985) ionization equation). The ratio of line emissivities, calculated by summing together contributions from two close Mg VI lines at 349.17 and 349.18 Å, and two Ne VI lines at 562.71 and 562.80 Å, at their temperature of maximum ionization fraction, varies somewhat with density (Figure 6). The variation is by no more than 15% over the expected (or measured) range of TR densities in our sources, of 10^9–10^{10} cm^{-3}. However we must have a means of measuring density.

The density can be derived from a diagnostic formed by the lines of Mg VII at 319.0 and 367.7 Å. Although this diagnostic is for slightly higher temperatures ($\log_{10} T_e = 5.8$) than the formation temperature of the Mg VI and Ne VI

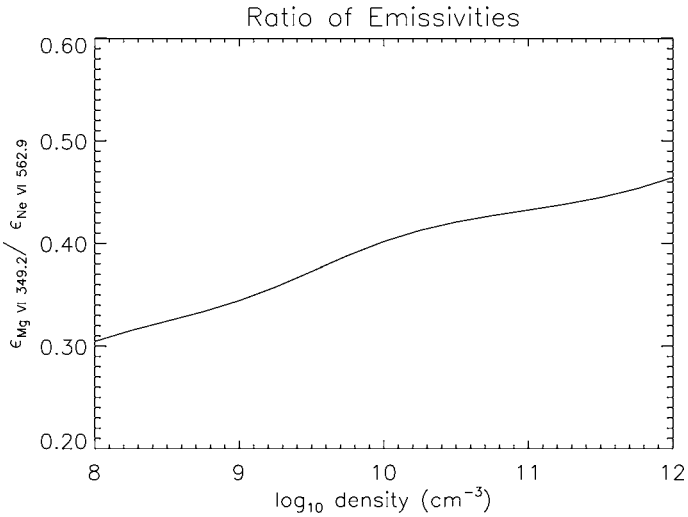

Figure 6. The variation with electron number density of the theoretical emissivity ratio ($\Delta E n_i A_{ji}$) in the Mg VI 349.16 + 349.18 Å lines and the Ne VI 562.7 + 562.8 Å lines, calculated using atomic data from the CHIANTI (v2.0) database.

ions ($\log_{10} T_e = 5.6$), there is a strong Mg VII component at the locations of the Ne VI/Mg VI sources, and we expect it will give a good idea of the local density. The theoretical density dependence of the Mg VII ratio is shown in Figure 7. Mg VII 367.7 Å is close to the stronger Mg XI line at 368.1 Å and must be fitted simultaneously with a double Gaussian. Mg VII 319.0 Å appears well-separated, but is blended with a strong high-temperature line of Ni XV (2.5 MK). Therefore, it can only be measured with confidence in regions where high temperature emission is negligible. The derived value of the density for Feature D, which is also the site of (overlying) emission in SXT and Si XII wavelengths, is therefore an upper limit. It should further be noted that if the TR is not homogeneous, the result of the density diagnostic will be biased towards values representative of the densest parts, and is thus an upper limit to the range of densities present (Almleaky, Brown, and Sweet, 1989).

The Mg/Ne intensity ratios in Features A–E are presented in Table III, along with the Mg VII intensity ratio, the electron density and the ratio of Mg to Ne abundances. Note, the errors on densities and abundances are as follows: densities have a blanket 25% error value, to take into account the expected theoretical unknowns in the atomic data, which are typically greater than the observational error. Observational errors are of the order 10–15%, combining the shot noise on the data, and a certain leeway in the fitting. The fitting algorithm is a χ^2 minimization algorithm, however there are cases where, for example, this results in a clear overestimate of background, and the fit is adjusted by hand. Also, abundances have a 25% blanket error, for the following reasons. Errors in the density lead to a typical 5–10% error in emissivity ratio read from Figure 7, as do errors in fitting the line intensities.

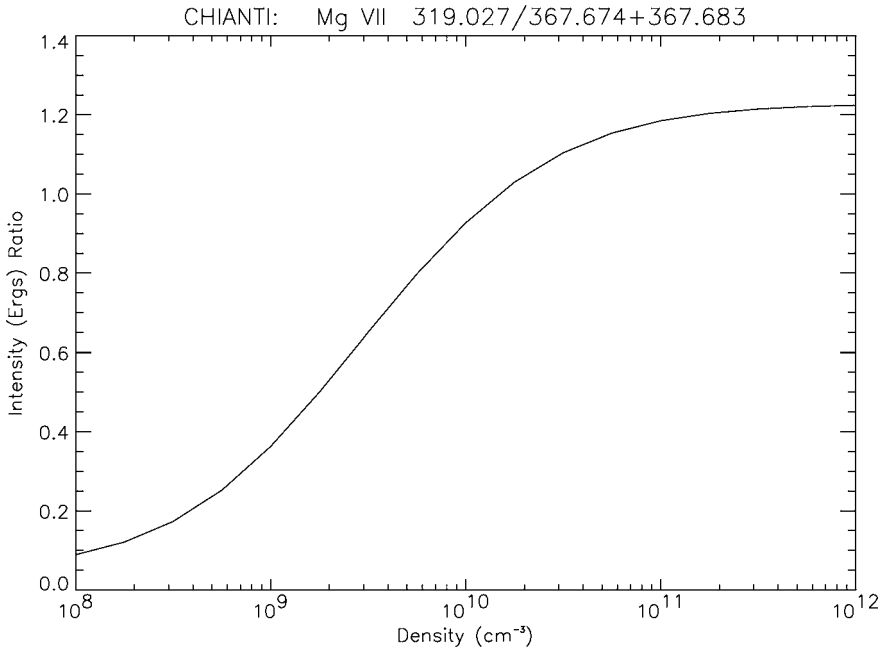

Figure 7. The Mg VII intensity ratio as a function of electron number density, at a temperature of 0.63 MK as predicted with atomic data from the CHIANTI (v2.0) data base.

However, these are smaller than the $\sim$ 15% theoretical error on both the numerator and the denominator in the emissivity ratio in (5). Combining errors gives 20–25%. It should be noted, however, that as these errors are predominantly due to theoretical unknowns in the atomic data, even if they were to reduce we would expect the trends in the abundance ratios to be preserved (see also Section 6).

The intensity values are calculated using the updated CDS NIS detector calibrations of 23 December 1998. This contrasts with the density and abundance values calculated by Young and Mason (1997) since that work dates from before the new detector calibrations were announced. The abundance values calculated using the new calibrations are roughly 0.6–0.7 times that of the values which would be calculated using the old values (dependent on electron density in the feature).

3.4. Evolution of Mg/Ne abundance ratios

Our derived abundance ratios range between 1 and 3. In none of the features is the abundance ratio $R_{\mathrm{Mg/Ne}}$ as low as the photospheric value reported as 0.26 ± 0.05 by Young and Mason (1997) in a low-lying TR feature, which they associated with flux emergence. The coronal ratio found by Young and Mason (1997) was 2.4 ± 0.3 with the old calibrations, or $\sim$ 1.7 with new calibrations. Our abundance values are thus all nearer coronal than photospheric values. Densities in each of the features,

TABLE III

Mg VI/Ne VI ratio, Mg VII density diagnostic ratio, electron number density, in units of 10^9 cm^{-3} and Mg/Ne abundance ratio on 3, 4 and June. For a given feature on 3 June, the first line is at 14:09:19 UT and the second line at 15:39:10 UT, for 4 June at 12:16:58 UT and 14:11:26 UT, for 5 June at 12:36:33 UT and 15:02:13 UT, respectively.

Date	Feature	$\frac{I_{349.2}}{I_{562.8}}$	$\frac{I_{319.0}}{I_{367.7}}$	$n_e(10^9\text{cm}^{-3})$	$\frac{Ab_{Mg}}{Ab_{Ne}}$
3 June	A	1.44 ± 0.10	0.65 ± 0.10	3.2 ± 0.8	3.2 ± 0.8
	A	0.97 ± 0.07	0.80 ± 0.18	5.7 ± 1.4	2.0 ± 0.5
	C	1.07 ± 0.12	0.71 ± 0.09	4.1 ± 1.0	2.3 ± 0.6
	C	1.53 ± 0.17	0.74 ± 0.08	4.7 ± 1.2	3.2 ± 0.8
	E	1.11 ± 0.08	0.64 ± 0.07	3.1 ± 0.8	2.5 ± 0.6
	E	1.78 ± 0.13	0.57 ± 0.09	2.4 ± 0.6	3.9 ± 1.0
	D	0.56 ± 0.08	0.78 ± 0.09	5.3 ± 1.3	1.2 ± 0.3
	D	0.59 ± 0.08	0.57 ± 0.08	2.4 ± 0.6	1.3 ± 0.3
	B	0.77 ± 0.06	0.55 ± 0.08	2.2 ± 0.5	1.7 ± 0.4
	B	0.80 ± 0.06	0.62 ± 0.11	2.9 ± 0.7	1.7 ± 0.4
4 June	B	0.9 ± 0.02	0.7 ± 0.02	3.2 ± 0.8	1.1 ± 0.3
	B	0.6 ± 0.02	0.6 ± 0.02	2.4 ± 0.6	0.7 ± 0.2
5 June	B	0.6 ± 0.02	0.6 ± 0.04	2.4 ± 0.6	0.8 ± 0.2
	B	1.0 ± 0.03	0.6 ± 0.02	3.0 ± 0.8	1.2 ± 0.3

from the Mg VII density diagnostic, are consistent with normal coronal values of a few $\times 10^9$ cm^{-3}.

Between the two 3 June rasters there are considerable changes in the value of the average abundance ratio, the most striking being the increase in the ratio in Feature C from 2.3 ± 0.6 to 3.2 ± 0.8, and in Feature E from 2.5 ± 0.6 to 3.9 ± 1.0. In the former case, the change is associated with evidence of heating, contrary to Feature E, where $R_{\text{Mg/Ne}}$ increases apparently without any heating taking place. There may in fact be some cooling. In Features B and D the abundances remain more-or-less the same, as do the ratios of intensity in the Ne lines. Note that in Feature D there is co-spatial high temperature emission which may have resulted in artificially high density measurements. This in turn may have led to the emissivity ratio being overestimated by $\sim 15\%$, and the abundance ratio underestimated by a corresponding amount.

On 4 and 5 June, $R_{\text{Mg/Ne}}$ for the single feature (which would correspond to Feature B) varies strongly, first decreasing from 1.1 ± 0.3 to 0.7 ± 0.2 on 4 June, then increasing from 0.8 ± 0.2 to 1.2 ± 0.3. The increase is associated with an increase in temperature, as shown by the ratio of the low-T Mg and Ne lines.

In summary, from feature to feature (and also within features, though we do not illustrate this here) there is no apparent correlation between n_e and the abundance ratio, neither do the rapidly varying abundance ratios systematically track temperature variations. But there are considerable abundance variations (though errors are large, they are due in a large part to atomic physics unknowns, and we expect that should these be resolved the trends we see would persist, with smaller errors - see Section 6). We wish to stress in particular that, out of all the features observed on 3 June, B and D are the ones having the lowest abundance ratio on both rasters. In Section 5, we attempt an explanation of this fact based on the results of our topological analysis (Section 4.3).

3.5. Determination of Mg/Ne abundance ratios using emission measures

The abundance variations between sources derived above are not large, and it is possible that they are an effect of temperature. Recall that in using the line ratio method we assume that the form of the $G(T)$ curves for each ion is sufficiently similar that the contributions as a function of temperature to the total emission are distributed in the same way. This is not the case; over the temperature range $\log_{10}(T_e) = 5.2$ to 5.8 the ratio $G(T)_{\mathrm{Mg\,VI}}/G(T)_{\mathrm{Ne\,VI}}$ varies between 0.4 and 1.5. However, we can examine the influence of temperature by looking at the emission over a number of lines formed at a range of temperatures.

If we assume that a spectral line is emitted over a temperature range ΔT around its temperature of peak formation $T_{\max}$, then we can approximate $G(T) =$ constant $= G_0$ in Equation (4). G_0 is defined as:

$$G_0 = \frac{\int G(T)\,\mathrm{d}T}{T(10^{0.15} - 10^{-0.15})} = \frac{\int G(T)\mathrm{d}T}{0.7\,T_{\max}}. \tag{6}$$

Then $I(\lambda)$ is directly proportional to the product of column emission measure and abundance, as follows.

$$4\pi I(\lambda) = Ab\ \Delta E G_0 EM, \tag{7}$$

where the column emission measure to depth L along the line of sight is defined as $EM = \int_L n_e^2\ \mathrm{d}s$. The EM derived at each temperature should be the same regardless of the ion which is being used to measure it. By comparing $Ab\ EM = 4\pi I(\lambda)/G_0\Delta E$ for a number of ions of Mg and Ne we see the effect of abundance. G_0 is calculated again using data from the CHIANTI database.

Plots of (scaled) $Ab\ EM$(T) are shown in Figures 8. These are divided according to the type of magnetic structure with which each is associated (which will be explained in Section 4.3). The difference between the two sets of curves for each source (Mg indicated by diamonds, Ne by triangles) reflects the effect of abundance.

Note, the expected dependence of EM on temperature (in a plane-stratified atmosphere where conduction balances radiation) is $EM \sim T^{3/2}$ (e.g., Jordan,

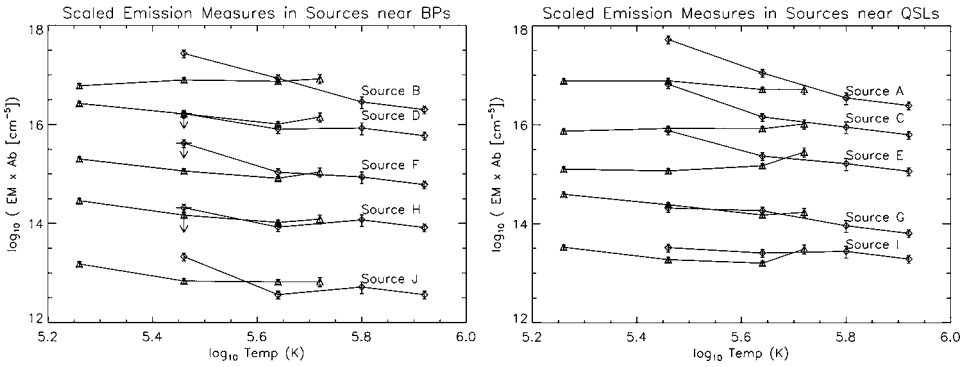

Figure 8. The (scaled) product of emission measure × abundance as a function of temperature, in various lines of Mg and Ne. The difference between the pair of lines for each source indicates the effect of abundance enhancements. Values for Mg are shown with *diamonds*, Ne is shown with *triangles*. Note that the values derived from Mg V (at $\log_{10} T_e = 5.5$) are upper limits in the case of Features D, F, G, and H, as the Mg V 353.3 Å line was too faint to fit reliably in these cases. The scaling is such that the y values for the bottom curve in each plot are equal to $\log_{10}(EM \times Ab/T^{3/2})$, and, to spread out the subsequent curves on the plot, the y values are at $\log_{10}(EM \times Ab/T^{3/2}) + 0.8, +1.6$, etc.

1996). We have removed this expected dependence by further dividing through by $T^{3/2}$; the purpose being only to emphasize the abundance variations. The abundance variations seen in this way are also small, however the fact that the lines for sources A, C, and E tend to be further offset from each other than those for B and D confirms our initial finding of abundance variations from source to source. The ratios $EM \times Ab$ for Mg VI and Ne VI, at $\log_{10}(T_e) = 5.6$ are in the range 0.8–2.8. These ratios are comparable to, but consistently lower than the abundance ratios found with the line ratio method, by a factor 1.4–1.6. Errors on the points shown are again a combination of measurement and atomic physics errors; the atomic physics errors lie in both the theoretical ionization fractions and the line emissivities. These combine to give errors of approximately 15%, comparable to the measurement errors.

The additional sources F-I shown on these figures are discussed Section 5.

4. The Magnetic Field Environment

4.1. Co-alignment of MDI and CDS images

We have co-aligned CDS and MDI, with the MDI images rotated to the start time of the CDS spectroheliograms. Generally, over the three analyzed days, the Si XII (2 MK) loops in the core of the AR begin and end around the strong leading bipole field but not in the very strongest longitudinal fields ($|B_l| > 500$ G), i.e., not in the sunspots. Rather, the core loops are rooted in weaker plage field of $100 < |B_l| < 500$ G. This agrees with similar results found by Golub, Zirin, and Wang (1994),

Schmieder *et al.* (1996) and Deng *et al.* (1999). Million degree emission in the lines of Mg IX and Ca X is concentrated in blobs around the ends of the Si XII structures. On 4 June, elongated million-degree structures – presumably loops – are clearly observed extending southwards from a region where negative and positive fields are in close proximity. This is also the location of a strong brightening in TR lines (Figure 10).

MDI movies of the local field (96 min synoptic cadence) indicate that TR brightenings take place under various conditions of the magnetic field. As an example of this variety, take the first CDS observations made on 3 June, at 14:09:19 UT, in the Ne VI 562.4 Å (Figure 9(a)). We pick three of the five identified brightenings, Features B, A, and D. Brightening B is in a region where positive spot field and negative plage field are close to one another. Brightening A is well inside the trailing positive polarity of the main bipole. The third brightening, D, is also in a positive field region which is in the process of dividing in two. It is, therefore, not clear that the brightenings are always related to flux emergence, for example, or always to magnetic cancellations at the photosphere.

4.2. Modeling the AR Magnetic Field

The magnetic field of the AR has been modeled in the linear magneto-hydrostatic (LMHS) approach. The equations governing the MHS equilibrium are:

$$\frac{1}{\mu_0}(\nabla \times \mathbf{B}) \times \mathbf{B} - \nabla p - \rho g \mathbf{u}_z = 0\,, \tag{8}$$

$$\nabla \cdot \mathbf{B} = 0\,. \tag{9}$$

Using a Cartesian system of coordinates, where z is the height above the photosphere (at $z = 0$) and (x, y) is the plane parallel to it, Low (1991) solved these equations writing the current density ($\mathbf{j} = \nabla \times \mathbf{B}/\mu_0$) in Equation (8) with Euler potentials. For any given function of the altitude $f(z)$, and taking α to be a constant (as in the linear force-free field, LFFF), the LMHS equilibrium condition can be rewritten as

$$\nabla \times \mathbf{B} = \alpha \mathbf{B} + f(z) \nabla B_z \times \mathbf{u}_z\,. \tag{10}$$

If $f(z) = 0$ we have the traditional LFFF equation; thus, the last term of Equation (10) takes into account the effect of the plasma pressure and gravity. From Equations (8) and (10), the plasma pressure and density can be expressed as

$$p = p_0(z) - \delta p = p_0(z) - f(z)\frac{B_z^2}{2\mu_0}\,, \tag{11}$$

$$\rho = \rho_0(z) - \delta\rho = -\frac{1}{g}\frac{\mathrm{d}p_0}{\mathrm{d}z} + \frac{1}{\mu_0 g}\left[\frac{1}{2}\frac{\mathrm{d}f}{\mathrm{d}z}B_z^2 + f(\mathbf{B}\cdot\nabla)B_z\right], \tag{12}$$

where $p_0(z)$ is independent of the magnetic field and varies only with z. It defines a background pressure (and density). Only the depletions δp and $\delta\rho$ depend on the magnetic field.

Equation (10) is solved using as boundary conditions the observed photospheric field (see Aulanier *et al.*, 1998b; Mandrini *et al.*, 1999b; López Fuentes *et al.*, 2000). Then Equations (11) and (12) give the pressure and density depletions as functions of the computed field. This procedure has the advantage of being applicable to observations, generalizing the LFFF approach. However, it cannot give a detailed description of the plasma properties since no input is allowed from the observed plasma parameters. Rather the function $f(z)$, together with the computed magnetic field configuration, give indirectly the plasma distribution (see Equations (11) and (12)). Following Low (1992), we have chosen $f(z)$ to be an exponential decreasing with height:

$$f(z) = a\ \exp(-z/H)\,, \tag{13}$$

where a and H are two parameters. Parameter a is the ratio between the pressure depletion δp and the magnetic pressure $B_z^2/2\mu_0$ (Equation (11)). The vertical extension of the influence of the plasma is given by the scale-height H. Low (1992) discussed in detail how H can be in some cases equal or close to an isothermal pressure scale-height. Here, we take $H = 5$ Mm as a typical pressure scale-height for plasma at a temperature of 10^5 K. Although the parameter a could be *a priori* estimated using pressure measurements, it is not obvious that the background pressure can be separated from the pressure depletion (see Equation (11)) in the observations. Moreover, the proposed solution (Equation (10)) is too simplified to take into account the large gradients observed in the temperature and density. We have chosen here $a = 1$, which is the maximum value allowed in the solution (see Aulanier *et al.*, 1998b). This value maximizes the effects of the plasma in the lower part of the atmosphere; for z of the order of or larger than H, the field is nearly force-free. We refer the reader to Aulanier *et al.* (1998b) for a discussion of the physical properties of this solution. More details about the behavior of pressure and density can be found in Low (1992). However, we would like to point out that the last term in Equation (12) is related to the curvature of the magnetic field, and that the density is higher in the presence of field lines that are curved upward (as is the case at BPs) than in the case of field lines curved downward (as in arcades). We use Equation (10) only to introduce, in a very simplified way, the perturbation to the classical LFFF model brought about by the plasma forces. For the transition region and the corona, these forces play a minor role and this solution may be used. In previous studies (Aulanier *et al.*, 1998b; Mandrini *et al.*, 1999b; López Fuentes *et al.*, 2000) it was found that a slightly better fit to the observations was obtained with this approach, while the basic results concerning the magnetic topology were similar to those given by a LFFF model. In the present case, we find that BPs and QSLs (see Section 4.3) appear at the same location in both models ($a = 0$ and

$a = 1$) for the same value of α; QSLs have the same extension, while BPs are slightly longer ($\approx 10\%$) in the LMHS model.

Once a and H are chosen, the model depends on the free parameter α. As a first approach, we have determined the value of α in such a way that the computed coronal field lines match (by an eyeball comparison) the shape of the loops observed by SXT in images taken on times close to the MDI magnetograms. The values of α that give the best fit to the observations are: $\alpha = 0.003$ Mm^{-1} for 3 June and 0.0045 Mm^{-1} for 4 and 5 June (Figure 2). Notice that the computed field lines follow the global 'S' shape of the SXT loops, however, α takes very low values. The observed 'S' shape may in fact, not be an indication of twist, rather of complexity in the photospheric field distribution. The configuration results from the combination of two sets of loops, i.e. it is not a single set of loops which have an 'S' shape. A similar configuration is also found with a potential extrapolation ($a = 0, \alpha = 0$; this implies that there are no currents in the coronal field).

We have also investigated whether the value of α could vary with height. We have found that, in order to fit the shape of chromospheric fibrils (see Figure 3), we have to increase the value of α up to 0.0075 Mm^{-1} for the three days. Doing so, the shorter SXT loops concentrated in the core of the AR (see Figure 4) were also better represented, the same being true for the Si XII brightenings shown in Figures 9 and 10. Similar results, showing that the magnetic shear may decrease with increasing height, have been found by Schmieder *et al.* (1997). They showed that, to fit the shape of observed loops, field lines computed at low coronal or chromospheric heights needed a higher α than those at higher heights.

4.3. Magnetic topology

Following the method of Démoulin *et al.* (1997), we have computed the locations of QSLs and analyzed their relationship to the observed CDS transition region brightenings. In previous papers QSLs were defined in terms of the norm of the displacement gradient tensor, but recently Titov, Démoulin, and Hornig (1999) have introduced a new geometrical measure of QSLs giving a mathematically more grounded definition. The application of this new definition to observations has not yet been implemented. However, it is expected that the spatial location of QSLs in theoretical configurations is the same for both definitions of QSLs; therefore, we apply here the earlier method which has shown to yield good accuracy when applied to observations (see references in the Introduction). QSLs are regions where field lines initially close together separate widely when followed. At the location of separatrices, the magnetic field line linkage is discontinuous, QSLs are a generalization of the concept of separatrices to configurations without such discontinuities. Therefore, when QSLs are computed we also find the places where separatrices will lie. Separatrices are present in the solar atmosphere in two cases, either when magnetic nulls appear in the configuration or when some field lines are tangentially touching the photosphere (these field lines are curved up at

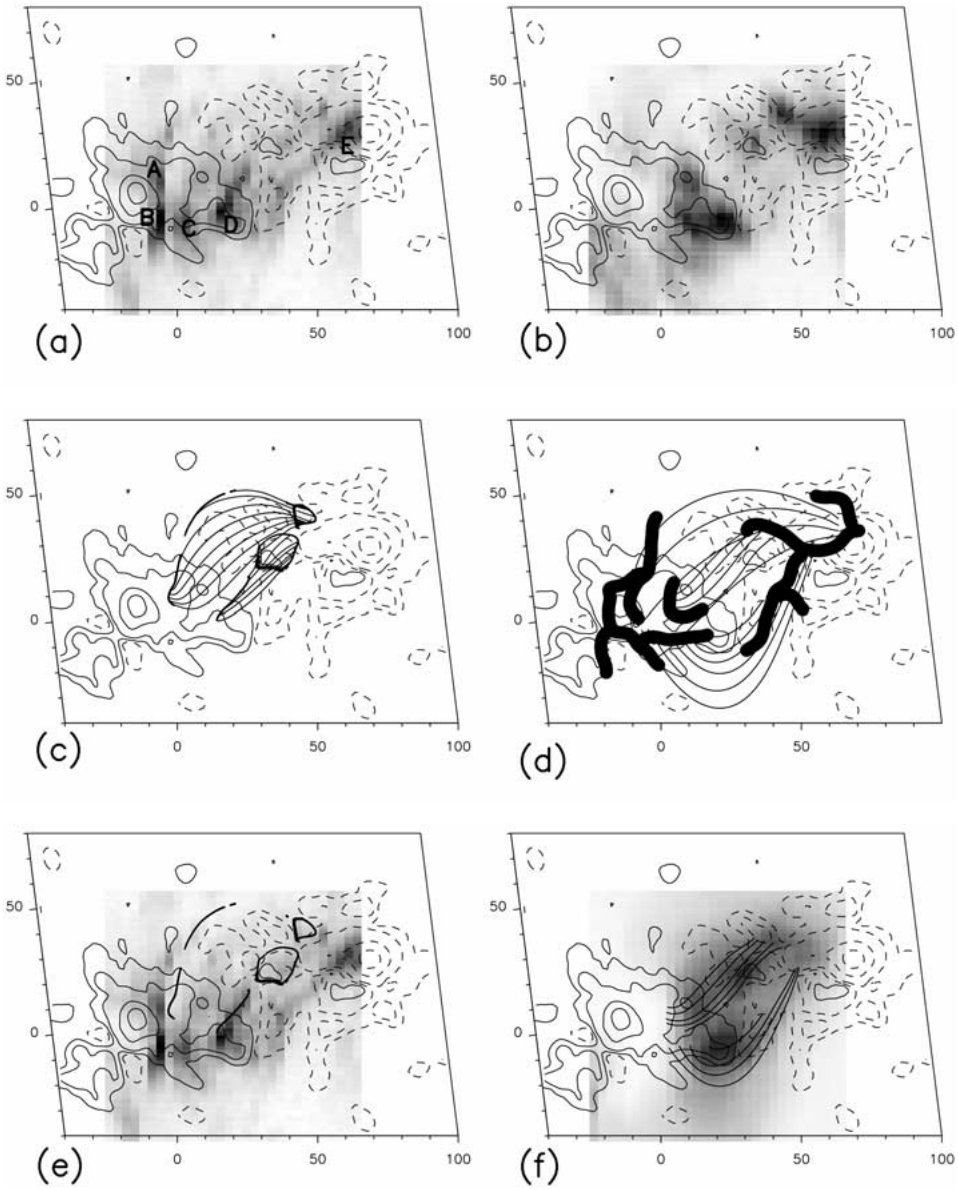

Figure 9. A comparison of the magnetic topology and CDS data for 3 June. (a) and (b) are, respectively, an overlay of Ne VI and Mg IX (reversed images) observations at 14:09:39 UT with the MDI magnetogram in Figure 2. In this case the iso-contours of B_l are $\pm$ 20, 100, 250, 500, 1000 G, positive (negative) values are drawn in *continuous (dashed)* lines. We have labeled the Ne VI features in (a). (c) shows the locations of BPs, and the intersection of their separatrices with the photosphere. BPs (separatrices) are drawn in *continuous thick (thin)* black lines, associated field lines have been added. (d) shows the intersection of QSLs (*thick lines*) with the photosphere, some field lines issued from QSLs are drawn. Note that, to keep (d) simple, BPs and BP separatrices shown in (c) have not been drawn - even though separatrices are a subset of QSLs (see text). In (e) we show only the BPs and their separatrices to point out their closeness to Ne VI brightenings, while in (f) it can be seen how the lines issued from the QSLs lying close to the Mg IX emission outline the shape of the Si XII emission (overlaid reversed image) at the core of the AR. The convention for the size and shape of the frames is the same as in Figure 2.

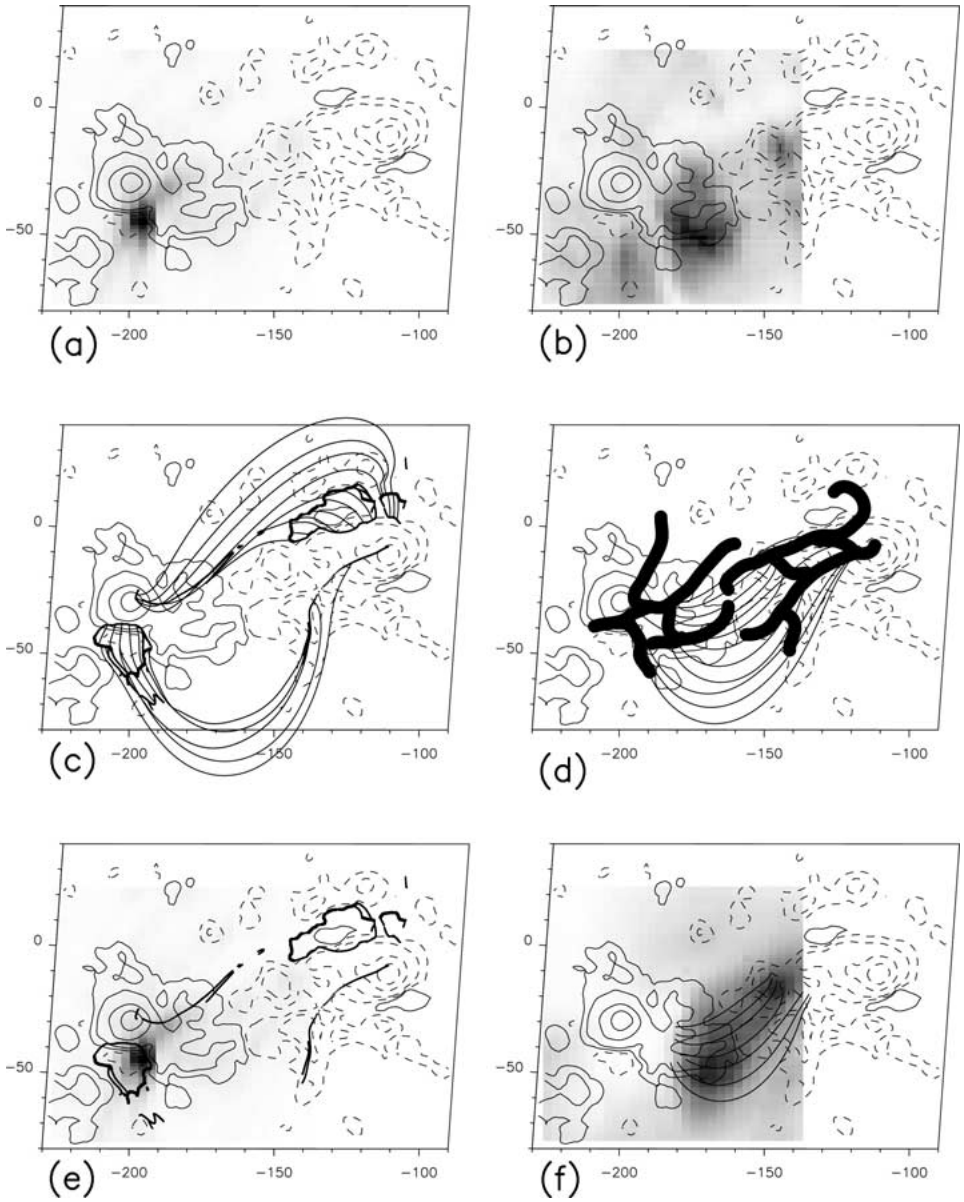

Figure 10. Same as Figure 9 for 4 June. Notice, when comparing (c) to (d), that some portions of the QSLs shown in (d) do overlay with the BP separatrices shown in (c). Compared to Figure 9, we have used a different criterion for choosing which QSLs to plot, as is discussed in the text.

the photosphere). This latter case can happen along portions of the inversion line for the component of the field normal to the photosphere. These portions are called BPs.

Figures 9 and 10 (and a corresponding one for 5 June, not shown) show that the topological structure of the AR is globally similar over the three analyzed days. QSLs located on the main bipolar field exhibit similar features from day to day. Differences in their distribution are mainly due to the appearance and/or evolution of parasitic polarities. While all separatrix structures are a subset of the QSLs, we remark that, to avoid overcrowding Figure 9(d) we have not included the sections of QSL which correspond to BPs and BP separatrices (compare Figures 9(c) and 9(d)). However, in Figure 10(d) some portions of the drawn QSLs *do* correspond to BP separatrices (those that overlay); we have included these here to show the relationship of the southern BP (not present on 3 June) and its separatrices to the QSLs located at the same place, and also (mainly at the place of the northern BP separatrices) to keep a coherent continuous pattern in the QSL drawing.

BPs are located mainly in two different regions: one, apparent on all days, at the north-east of the leading spot (these we refer to as the northern BPs), and the other, only appearing on 4 and 5 June, at the south of the following spot (the southern BPs); see Figures 9(e) and 10(e). The location and shape of these BPs change according to the evolution of the moving magnetic features in the moat of the leading spot. The separatrices associated with the northern BPs are, on the west side of the BPs, very close to them (lying at a low field region with $|B_l| \approx 20$ G, see Figures 9(c) and 10(c)); while they extend farther away towards the east (up to the zone with $|B_l| > 500$ G). On 4 and 5 June the separatrices corresponding to the southern BPs lie on the low field region ($|B_l| \approx 100$ G) below the following spot, and along the negative field region which extends south–east from the preceding spot. On 3 June there is also a central BP, having one of its separatrices extending in the NW-SE direction (see Figure 9(c) and Section 4.4). This particular BP is significant in our interpretation of the CDS TR brightenings and abundance variations.

On 3 June, we do not find a BP at the corresponding location of the 4 June and 5 June southern BPs (Figures 9(e) and 10(e)), though QSLs resembling the shape of the southern BPs separatrices are present (Figures 9(d)). We find that from 3–4 June the positive polarity decreased in flux, while the negative one increased. This change in the relationship between positive and negative flux from 3–4 June is the origin of the appearance of the southern BPs. Nevertheless, we suspect strongly that in reality a BP was present there on 3 June, for the following reason. When a parasitic polarity is present in a surrounding field of opposite polarity, the size of the magnetogram pixel has a dramatic effect: there is not only an averaging of the magnetic intensity, but also a cancellation of the parasitic flux with the neighboring stronger field, since what is measured is the magnetic flux. This effect can delay the appearance of a parasitic polarity in the magnetogram by more than one day

(as in the flaring configurations studied by Mandrini *et al.*, 1993; Aulanier *et al.*, 1998b).

4.4. Relationship between CDS brightenings and magnetic topology

Figures 9 and 10 illustrate the relationship between the locations of BP separatrices or QSLs and Ne VI, Mg IX or Si XII brightenings on 3 and 4 June (both observations and magnetic field topology are very similar between 4 and 5 June). We have chosen Ne VI, Mg IX, and Si XII for our comparison, due to their difference in formation temperature. Ne VI (respectively, Mg IX) emission mainly comes from the low (respectively, high) TR, so we expect to observe kernels in these lines close to the footpoints of the magnetic field lines; while, Si XII emission is associated with their coronal portion (see Section 3). In order to simplify the figures we have drawn QSLs and BPs, together with their separatrices, only when they lie within the CDS field of view, and occur near the observed CDS emission.

The presumed footpoints of the hot emission seen in Si XII lie near the core of the AR, from the evidence of Mg IX 1 MK emission (Peres, Reale, and Golub, 1994; Berger *et al.*, 1999). As shown in Figures 9 and 10 (panels b and d), we find QSLs lying close to the Mg IX brightenings (see also Figure 11); furthermore, the global shape of the coronal Si XII and SXT emission coincides with the shape of field lines which have footpoints at these QSLs. We also observe that the more diffuse SXT (see Figures 4) emission can be traced by field lines which have footpoints at the QSLs located on the main bipolar field. So the intense core Si XII emission (outlining the 2 MK plasma) and soft X-ray emission (outlining the 2–6 MK plasma), may be due to energy release at QSLs where current sheets form and heating is likely to take place. Differences in intensity between the core and diffuse SXT emission may be linked to the volume of the magnetic flux tubes involved, and the amount of energy released.

Mg IX and Si XII emission is not observed associated with all separatrix or quasi-separatrix structures. Whether or not it is so may also depend on whether the energy released at reconnection occurring at these structures is enough to heat corona and transition region to sufficiently high temperatures.

Turning now to the cooler emission in the bright Ne VI features, we see that there is a general coincidence in position between these features and the positions of either the intersection of QSLs with the photosphere, or the intersection of separatrices issuing from BPs with the photosphere (note, not at the BPs themselves). Close inspection shows that many of the dimmer elongated features on the Ne VI map are also very near QSLs or BP separatrices; compare Figures 9(a), 9(c–e) and Figures 10(a), 10(c-e).

In particular, on 3 June, Feature D lies directly on top of a BP separatrix from the central BP. The central BP and its separatrix disappear the next day along with feature D. This provides strong evidence for a link between Feature D and the

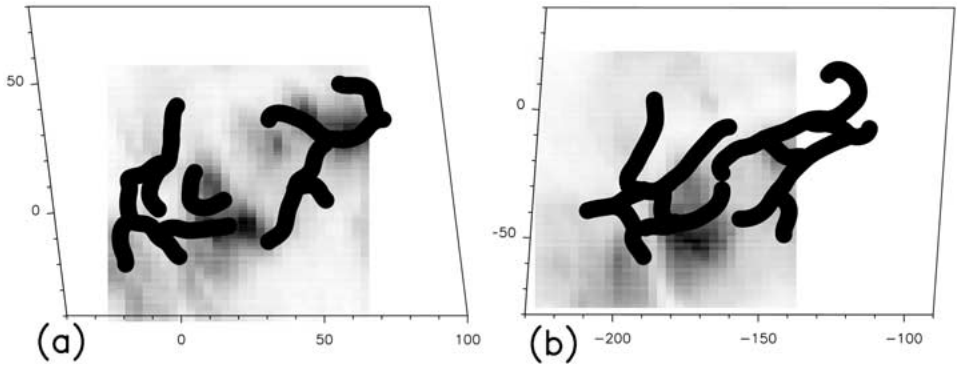

Figure 11. The positions of the photospheric intersections of QSLs overlaid on CDS Mg IX emission, on (a) 3 June and (b) 4 June. Certain of the QSL intersections overlie patches of Mg IX emission; those which do mark the footpoints of loops which are bright in Si XII and SXT.

central BP. Also, Feature B, though not obviously on a BP separatrix on 3 June, is at a location which on 4 and 5 June clearly shows a BP and separatrix structure, and a persistent Ne VI brightening. Section 4.3 explains why a BP may already be present on 3 June but not revealed by the extrapolations.

Feature A on 3 June lies close to a separatrix from the north-east BP, and directly on top of a location where QSL field lines intersect the photosphere. Features C and E are close to locations where QSLs intersect the photosphere. Displacements between the BP separatrices or QSLs and the brightenings may have three different origins: an error in the co-alignment between CDS and MDI, an error in the computed coronal field, or a physical displacement of the TR features from the BP separatrices or QSLs, as a result of connectivity changes following reconnection. CDS pointing accuracy is not guaranteed to better than $\sim$ 5 arc sec in the x and y directions combined; this is a reasonable estimate for the co-alignment error (equivalent to $\pm$ 3.6 Mm at disk center). It is difficult to quantify the error due to inadequate modeling of the coronal magnetic field. The value of α, which is the main free parameter in our model, is estimated from the overall comparison of computed field lines to observed loops, and local differences might be present (a non-linear force free model would give a better answer when transverse field measurements are available). For AR 8048, we have found that changing α in the LMHS model by $\pm$ 25% implied a shift in the QSLs or BP separatrices of at most 5 Mm in regions where the magnetic field stays below $\approx$ 200 G. Concerning our third source of error, the displacement between footpoints of field lines before and after reconnection can be quite remarkable in the case of very energetic events (i.e., in two-ribbon flares), but in this particular study, we are dealing with low energy events and we do not expect that the TR brightenings displace much more than our co-alignment error as reconnection proceeds.

Summing up, we suggest that many of the bright TR brightenings visible in the Ne VI raster are associated with the intersection of various topological structures

with the photosphere. We have found two types of structures; those composed of field lines issuing from a photospheric bald patch, and the more general quasi-separatrix layers (the ones which are not associated with BPs). Features B and D are probably linked to BP separatrices; while Features C, E and some weak emission surrounding Feature B on 4 and 5 June are related to QSLs. Feature A can be linked to either a BP separatrix or to a QSL, as explained above. Features C and E are at the base of large, diffuse SXT loops extending out into the corona and are, thus, consistent with the nature of the Sheeley features and those observed by Young and Mason (1997).

5. Origin of the Ne VI Brightenings and Abundance Variations

The results described above lead us to propose the following physical scenario. Ne VI features are in general a consequence of energy release by magnetic reconnection at separatrices, driven by the continual magnetic field changes observed. Features B and D (and possibly A) are the consequence of energy release by magnetic reconnection occurring at the BP separatrices (considering that on 3 June Feature B is probably also associated with a BP and its separatrix - see the end of Section 4.3). Features C, E and probably A lie close to the photospheric intersection of QSLs. These brightenings may result from magnetic reconnection at the related QSLs.

The BPs themselves are also locations in which reconnection will occur, but this occurs at a very low height in the atmosphere (chromospheric or even photospheric) and, thus, we might not expect to see TR brightenings right above the BPs. But during BP reconnection, two things might happen. Firstly, part of the energy released is transported along separatrix field lines, as particles or in the form of conduction, causing heating and the evaporation of some chromospheric plasma at the other end. This may cause local brightenings. But secondly, in the post-reconnection configuration at BPs, in which field lines which were tangent to the photosphere at the BP and concave up (see, e.g., Titov, Priest, and Démoulin, 1993) spring up after reconnection, photospheric material can then be lifted into the atmosphere by the rising BP field lines, and spread out along them. Thus one would expect field lines associated with BPs to exhibit a more photospheric abundance ratio than those which are not.

We do indeed observe a difference in the abundance ratio Mg/Ne between the different sources, and suggest that this may be linked to the different ways magnetic reconnection proceeds in QSLs and BPs. We have found that both Features B and D (associated to BPs) have somewhat lower abundance ratio when compared to typical coronal abundances, while other features (C, E), which are associated with QSLs, have an abundance ratio around the typical coronal value.

The status of feature A is unclear. It is close to both a QSL intersection and a BP separatrix, though closer to the QSL location. If indeed it is associated with

a BP separatrix, rather than the nearby QSL, then we must explain why its abundance ratio is higher than the BP sources B and D. Is source A an exception to the association of BPs with low abundance ratios? One explanation may lie in the height of the field lines connecting the BP and the location of the intersection of its separatrix with the photosphere near Feature A. These field lines are long and high, compared to the equivalent field lines ending near sources B and D. The lift-up and transport along the field lines in BP reconnection is likely to be more efficient in short, low-lying magnetic lines.

Broadly speaking, it is seen that the Mg/Ne abundance ratio is less than 2 for sources associated with BPs, and greater than 2 for sources associated with QSLs. The small number of sources, A to E, had been identified and studied before the field topology was investigated, but this hint of a relationship between topological structures and abundance ratio prompts us to look at the abundances at fainter sources, coincident with other predicted QSL and BP separatrix structures on 3 June - the full set is indicated on Figure 12.

We have defined a further 5 sources in which the Ne VI (562.8 Å) intensity is greater than 20 ergs cm^{-2} s^{-1} $sterad^{-1}$. Using the same analysis method described earlier we find that in another three sources (F, H and J) close to BP separatrix locations $R_{Mg/Ne}$ is again less than 2. The values are $R_{Mg/Ne} = 1.7 \pm 0.5$, 1.2 ± 0.3 and 0.8 ± 0.2, respectively. Two further sources, G and I, close to QSLs show (for I) $R_{Mg/Ne} = 2.7 \pm 0.6$, in line with previous examples, and (for G) $R_{Mg/Ne} = 0.9 \pm 0.2$, which does not follow the trend. However, it should be noted that this latter source is also at the location where a BP and BP separatrix appear on the following day, and we may have a situation similar to that of the much stronger source B, which had a low abundance ratio the day before the BP appeared in the computations. With the exception of source G, the ratio of $EM \times Ab$ for Mg VI and Ne VI is again consistently lower by a factor 1.4–1.6 than the abundance ratios found using the line ratio method.

The abundance variations were also studied at different temperatures, as in the case of brightenings A–E. The results are summarized in Figures 8(a) and 8(b) which are plotted for BPs and QSLs respectively. Although the differences between the two plots are not large, consistent with the fact that the abundance variations from the line ratio technique are not large, it should be noted that there is a general trend for the Mg and Ne curves (diamonds and squares) to be closer together in the sources near BPs than those near QSLs. This effect is in fact more prominent than the figures show. The values on the Mg curves at $\log_{10} T_e = 5.5$ (Mg V) are upper limits in Features D, F, and H (and also in Feature G, which further adds to our suspicion that this was a forming BP separatrix on 3 June), since the Mg V line was too faint to measure reliably. This would bring the curves yet closer together in 3 of 5 of the BP features, as well as Feature G. This further analysis supports our contention that the abundance ratios are systematically different near BPs and QSLs, with BPs showing a lower ratio of low to high FIP elements – more photospheric – and QSLs showing a higher ratio.

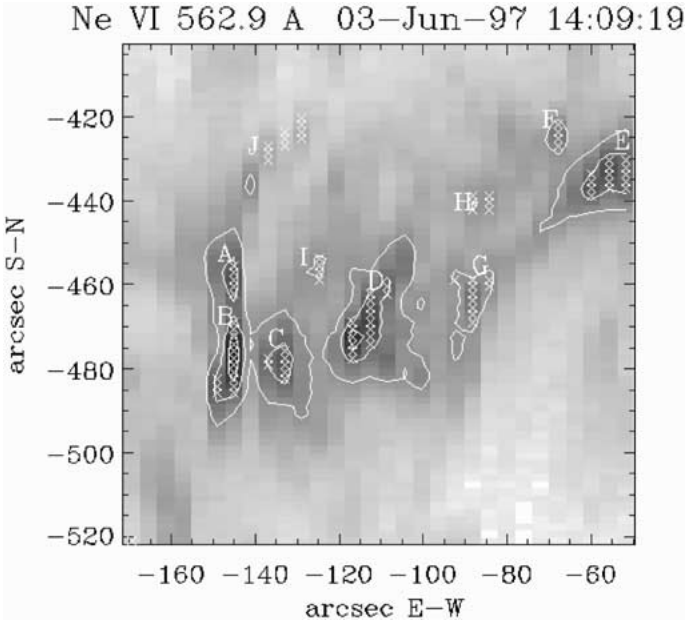

Figure 12. The full set of sources for which abundance measurements were made.

6. Conclusion

We have presented the analysis of AR 8048 during three days using coordinated observations of SOHO (CDS and MDI), *Yohkoh* (SXT) and Bialków (Hα telescope). They provide several diagnostics (temperatures, densities, abundances) of the TR and coronal plasma, the longitudinal component of the photospheric field and chromospheric brightness distribution.

At transition region temperatures, this AR presents five main bright features on 3 June, while only one is observed on the next two days. Densities in the strong Ne VI features, measured with CDS line ratio diagnostics, are consistent with normal TR values and remain constant from pixel to pixel, within the errors. Features A, C and E have Mg/Ne abundance ratio as high as previously measured for coronal structures, while features B and D have a somewhat lower abundance ratio (but still above typical photospheric values). The average Mg/Ne abundance ratio in bright sources, varies with time by up to 80%, and there are also pixel-to-pixel variations in the ratio. The elemental abundance ratios have long been known to vary in solar flares (cf., Lin, 1987) and it has been proposed, for example, that selective acceleration of ions on the basis of charge-to-mass may occur by waves generated in reconnection events (Miller and Viñas, 1993). We propose an alternative, linked to magnetic reconnection.

The co-alignment of the CDS and *Yohkoh* data with MDI, together with the computation of the coronal magnetic field and its topology have shown the re-

lationship between the emissions at various temperatures (TR and coronal), and the magnetic field topology. At coronal temperatures, the Si XII emission, at the core of the AR, is related to the high transition region Mg IX brightenings lying on QSLs (quasi-separatrix layers). Field lines starting from these QSLs follow the shape of the Si XII emission. The most diffuse SXT emission is also related to magnetic lines linking QSLs at the main bipolar field. Many features which are bright in the TR line of Ne VI lie close to the photospheric intersection of topological structures, both bright point (BP) separatrices and QSLs. These topological structures are locations where energy release is likely to take place, in the form of heating at current sheets for example. The narrow, elongated appearance of the TR brightenings is consistent with the photospheric intersection of these structures. The disappearance of one of the TR features, feature D, is simultaneous with the disappearance of its associated BP and BP separatrix.

We have further noted abundance differences between the TR features observed in Ne VI, and suggest a possible origin for this. Features C, E, and (most likely) A are found to be associated with QSLs and have $R_{\mathrm{Mg/Ne}} > 2$. These TR and coronal brightenings have most probably their origin in the release of magnetic energy by reconnection at the QSLs, as described in the model of Démoulin and Priest (1997). Features B, and D are rather found associated with a particular magnetic topology formed by field lines which are tangent to and curved up above the photosphere (at BPs). Both Feature D and the corresponding BP, present on 3 June, disappear the next days. Magnetic reconnection in a BP topology, not only releases energy, but allows the lifting-up of photospheric or chromospheric material (e.g., Titov, Priest, and Démoulin, 1993; Cheng and Choe, 1998) which has typically a lower abundance ratio than coronal plasma. The action of BP reconnection may therefore lead to the more chromospheric abundance ratio observed in BP-associated brightenings. The observed differences in abundance ratio between features may therefore be due to the magnetic topology involved. This tendency is broadly confirmed by a further four fainter sources (F to I). It should be noted that in source G, apparently associated with a QSL, the abundance ratio is low. However, the following day, a BP separatrix has appeared at the same location.

It must be noted that, mostly due to unknowns in the theoretical atomic data, the errors on the abundance values are large - in many cases comparable to the differences between abundance values measured from source to source. So at the moment we can claim no more than a trend in the data. However, the theoretical unknowns are such that, should it be discovered that these unknowns have led to the emissivity values being wrongly estimated (for example) all abundance results from the line ratio technique would be affected in the same way. The trend in abundance ratios would be preserved and the errors reduced. Likewise with theoretical problems with the density Mg VII density diagnostic; all densities are currently all under- or all over-estimated, and again the trend in abundance ratios would remain were the atomic parameters to be corrected.

Until the errors in theoretical quantities are reduced, our best hope at a clear result associating abundance ratio with magnetic field would come if we could identify ARs in which much larger abundance variations are visible. Variations of up to a factor 10 have been found previously (e.g., Young and Mason, 1997), which are far beyond what could be explained by possible observational/theoretical unknowns. It is also certainly worthwhile analyzing a much larger set of events before drawing a firm conclusion, though if only weak abundance variations are seen again we are left facing the problem with atomic physics errors.

However, the present results can serve as a guide to constrain further the possible processes which may lead to an abundance segregation. There is further work to be done; for example, we observed a correlation between the increase of temperature and the abundance ratio in several cases. We end by making the point that existing models for FIP variations involve the local geometry of the magnetic field (in the region $T \approx 10^4$ K where the segregation occurs according to the FIP of the element), while the present results show that the magnetic topology – a global quantity – may also have an important role.

Acknowledgements

We wish to acknowledge useful discussions with Sarah Gibson and Dick Canfield, and the help of the SOHO-CDS team, in particular Dave Pike. We thank Pawel Rudawy for providing the Bialków observations and Yuan Yong Deng for data processing of Figure 3. We acknowledge financial support from ECOS (France) and ANPCYT (Argentina) through their cooperative science program (A97U01), and also from PPARC (UK). Part of this work (LF, NN) was carried out under NASA contact NS8-37334 (*Yohkoh*/SXT). SOHO is a project of international collaboration between ESA and NASA. The *Yohkoh* mission is a project of the Institute of Space and Astronautical Science (ISAS) in Japan. It is financially supported by ISAS, NASA and PPARC. The authors of this paper benefited from discussions at the second SOHO–*Yohkoh* Coordinated Data Analysis Workshop held in MEDOC, Orsay, France.

References

Almleaky, Y. M., Brown, J. B., and Sweet, P. A.: 1989, *Astron. Astrophys.* **224**, 328.

Aulanier, G., Démoulin, P., van Driel-Gesztelyi, L., Mein, P., and DeForest, C.: 1998a, *Astron. Astrophys.* **335**, 322.

Aulanier, G., Démoulin, P., Schmieder, B., Fang, C., and Tang, Y. H.: 1998b, *Solar Phys.* **183**, 369.

Aulanier, G., Schmieder, B., Kucera, T., van Driel-Gesztelyi, L., Démoulin, P., Mein, N., Vial, J.-C., and Mein, P.: 1999, in B. Schmieder, A. Hofmann, J. Staude (eds.), Third Advances in Solar Physics Euroconference: Magnetic Fields and Oscillations, *ASP Conference Series*, Vol. 184, pp. 291–295.

Arnaud, M. and Rothenflug, R.: 1985, *Astron. Astrophys.* **60**, 425.
Bentley, R. D., Klein, K.-L., van Driel-Gesztelyi, L. *et al.*: 2000, *Solar Phys.* **193**, 227.
Berger, T. R., De Pontieu, B., Schrijver, C. J., and Title, A. M.: 1999, *Astrophys. J.* **519**, L97.
Cheng, C. Z. and Choe G. S.: 1998, *Astrophys. J.* **505**, 376.
Delaboudinière, J. P., Artzner, G. E., Brunaud, J., Gabriel, A., Hochedez, J. F. *et al.*: 1995, *Solar Phys.* **162**, 291.
Démoulin, P. and Priest, E. R.: 1997, *Solar Phys.* **175**, 123.
Démoulin, P., Bagalá, L. G., Mandrini, C. H., Hénoux, J. C., and Rovira, M. G.: 1997, *Astron. Astrophys.* **325**, 305.
Deng, Y. Y., Schmieder B., Mandrini, C. H., Khan, J. I., Démoulin, P., and Rudawy, P.: 1999, *Astron. Astrophys.* **349**, 927.
Dere, K. P., Landi, E., Mason, H. E., Monsignori-Fossi, B. M., and Young, P. R.: 1997, *Astron. Astrophys.* **125**, 149.
Fletcher, L. and DePontieu, B.: 1999, *Astrophys. J.* **520**, L136.
Gaizauskas, V., Mandrini, C. H., Démoulin, P., Luoni, M. L., and Rovira, M. G.: 1998, *Astron. Astrophys.* **332**, 353.
Glover, A., Ranns, N. D. R., Harra, L. K., Culhane, J. L.: 2000, *Geophys. Res. Lett.* **27**, 2161.
Golub, L., Zirin, H., and Wang, H.: 1994, *Solar Phys.* **153**, 179.
Harrison R. A., Sawyer, E. C., Carter, M. K. *et al.*: 1995 *Solar Phys.* **162**, 233.
Hudson, H. S., Lemen, J. R., St. Cyr, O. C., Sterling, A. C., and Webb, D. F.: 1998, *Geophys. Res. Lett.* **25**, 248.
Jordan, C. E.: 1996, in S. Bowyer and R. F. Malina (eds.), *Astrophysics in the Extreme Ultraviolet*, IAU Colloquium 152, Berkeley, California, USA; Kluwer Academic Publ., p. 81.
Landi, E., Landini, M., Dere, K. P., Young, P. R., and Mason, H. E.: 1999, *Astron. Astrophys. Suppl. Series* **135**, 339.
Lin, R. P.: 1987, *Rev. Geophys.* **25**, 676.
Longcope, D. W.: 1996, *Solar Phys.* **169**, 91.
López Fuentes, M. C., Mandrini, C. H., Rovira, M. G., and Démoulin, P.: 2000, *Geofis. Inter.* **39**, 65.
Low, B. C.: 1991, *Astrophys. J.* **370**, 427.
Low, B. C.: 1992, *Astrophys. J.* **399**, 300.
Mandrini, C. H., Démoulin, P., and Klimchuk J.: 2000, *Astrophys. J.* **530**, 999.
Mandrini C. H., Rovira M. G., Démoulin P., Hénoux J.-C., Machado M. E., and Wilkinson L. K.: 1993, *Astron. Astrophys.* **272**, 609.
Mandrini, C. H., Démoulin, P., van Driel-Gesztelyi, L., Schmieder, B., Cauzzi, G., and Hofmann, A.: 1996, *Solar Phys.* **174**, 229.
Mandrini, C. H., Démoulin, P., Schmieder, B., Deng, Y. Y., and Rudawy, P.: 1999a, *ESA-SP* **448**, 617.
Mandrini, C. H., Deng, Y. Y., Schmieder, B., Démoulin, P., Rudawy, P., Newmark, J., and DeForest, C.: 1999b, *ASP Conf. Ser.* **184**, 276.
Meyer, J.-P.: 1985a, *Astrophys. Suppl. Series* **57**, 173.
Meyer, J.-P.: 1985b, *Astrophys. Suppl. Series* **57**, 151.
Miller, J. A. and Viñas, A. F.: 1993, *Astrophys. J.* **412**, 386.
Nakagawa, Y.: 1971, in Robert Howard (ed.), 'Solar Magnetic Fields', *IAU Symp.* **43**, 275.
Ogawara Y., Takano K., Kato T., Kosugi T., Tsuneta S. *et al.*: 1991, *Solar Phys.* **136**, 1.
Peres, G., Reale, F., and Golub, L.: 1994, *Astrophys. J.* **422**, 412.
Pevtsov, A. A., Canfield, R. C., and Metcalf, T. R.: 1995, *Astrophys. J.* **440**, L190.
Pevtsov, A. A., Canfield, R. C., and McClymont, A. N.: 1997, *Astrophys. J.* **481**, 973.
Rust, D. M. and Kumar, A.: 1996, *Astrophys. J.* **464**, L199.
Sakurai, T. and Wang, H.: 1999, in T. S. Bastian, N. Gopalswamy and K. Shibasaki (eds.), *Proceedings of the Nobeyama Symposium*, Kiyosato, Japan, October 27–30, 1998, NRO Report No. 479., pp. 77–81.
Scherrer, P. H., Bogart, R. S., Dush, R. J. *et al.*: 1995, *Solar Phys.* **162**, 129.

Schmieder, B., Démoulin, P., Aulanier, G., and Golub, L.: 1996, *Astrophys. J.* **467**, 881.
Schmieder, B., Aulanier, G., Démoulin, P., van Driel-Gesztelyi L., Roudier T., Nitta N., and Cauzzi G.: 1997, *Astron. Astrophys.* **325**, 1213.
Seehafer, N.: 1986, *Solar Phys.* **105**, 223.
Sheeley, N. R.: 1996, *Astrophys. J.* **469**, 423.
Titov, V. S., Démoulin, P., and Hornig, G.: 1999, in A. Wilson (ed.), Proc. of the Ninth European Meeting on Solar Phys., *ESA-SP* **448**, 715.
Titov, V. S., Priest, E. R., and Démoulin, P.: 1993, *Astron. Astrophys.* **276**, 564.
Tsuneta, S., Acton, L. W., Bruner, M. *et al.*: 1991, *Solar Phys.* **136**, 37.
van Ballegooijen, A. A., Nisenson, P., Noyes, R. W.; Löfdahl, M. G., Stein, R. F., Nordlund, Å., and Kishnakumar, V.: 1998, *Astrophys. J.* **509**, 435.
van Driel-Gesztelyi, L.: 1998, in C. E. Alissandrakis and B. Schmieder (eds.), *ASP Conf. Ser*. **155**, 202.
Wang, T., Wang, H., and Qiu, J.: 1999, *Astron. Astrophys.* **342**, 854.
Young, P. R. and Mason, H. E.: 1997, *Solar Phys.* **175**, 523.
Young, P. R. and Mason, H. E.: 1998, *Space Sci. Rev.* **85**, 315.